Exciton dynamics in self-assembled molecular nanotubes

Kriete, Björn

DOI:
10.33612/diss.123832795

Chapter 2

Experimental Methods

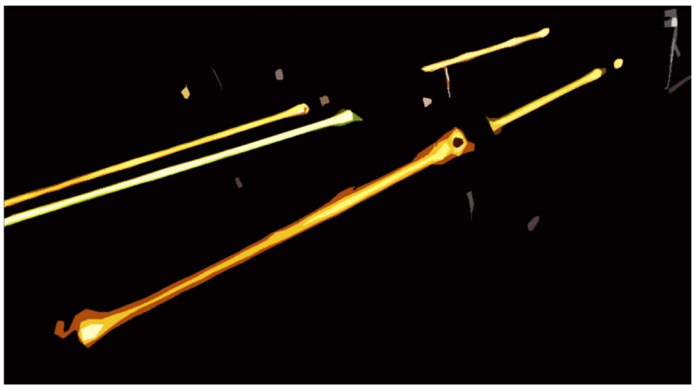

Optical spectroscopy – the science of light-matter interactions – is an equally elegant and powerful experimental tool to study the photophysical properties of (soft) condensed matter systems. For photoactive, multi-chromophoric molecular systems such as self-assembled nanotubes, spectroscopic observables can be used as highly sensitive reporters to answer a number of questions: What is the underlying molecular structure? How does the system evolve in its excited state following optical excitation? How does the system interact with its surrounding and dynamically fluctuating environment? And what are the relevant timescales for these phenomena? The full potential of optical (time-resolved) spectroscopy can be harnessed by combining it with complementary techniques including microscopy (optical and transmission electron microscopy) and microfluidics. The following section provides an overview of the experimental methods that are used in this Thesis with the focus on the concepts of the respective technique rather than the technical details; the latter are provided in the respective chapter.

Image: Photograph of the 2D spectrometer used in this Thesis.

2.1 Steady-State Spectroscopy

2.1.1 Absorption and Photoluminescence

Already simple steady-state linear UV-Vis absorption and photoluminescence (PL) spectroscopy can yield a wealth of information on the (optical) properties of a system, where the information is encoded in the general shape of the spectra[1]: occurrence and number of different peaks, peak shifts, (relative) peak amplitudes, lineshapes and linewidths, Stokes shift, *etc*. Typically, an absorption spectrum is measured by scanning the wavelength λ of the illumination source and recording the incident $I_0(\lambda)$ and transmitted intensity $I(\lambda)$ as shown in Figure 2.1a. The optical density (OD) of the sample is then computed as the logarithm of the ratio of these two intensities:

$$\mathrm{OD}(\lambda) = -\log_{10}\left(\frac{I(\lambda)}{I_0(\lambda)}\right) = \epsilon(\lambda)cd. \tag{2.1}$$

Here, ϵ is the extinction coefficient of the sample under study (a material property), c the molar concentration of the sample and d the thickness of the sample. It immediately follows from Eq. 2.1 that at high optical densities the intensity of the transmitted light becomes extremely low and, hence, difficult to measure. Typically, the upper limit of measurable optical densities of commercial absorption spectrometers is on the order of $\mathrm{OD} \sim 4$ corresponding to a sample transmission of 0.01 %. In many instances this requires either using a thinner sample/cuvette or diluting of the sample in order to obtain sufficiently low peak optical densities. On the other hand, as measurement of the absorption spectrum relies on measuring changes of the incident intensity ($I_0 - I_{\mathrm{abs}}$) at the background of the transmitted intensity (I_T), it a non-background-free technique, which directly imposes limits to its sensitivity. As a result, the optical density of the sample cannot be too low either, as otherwise $I_T \approx I_0$, for which the optical density becomes immeasurably low.

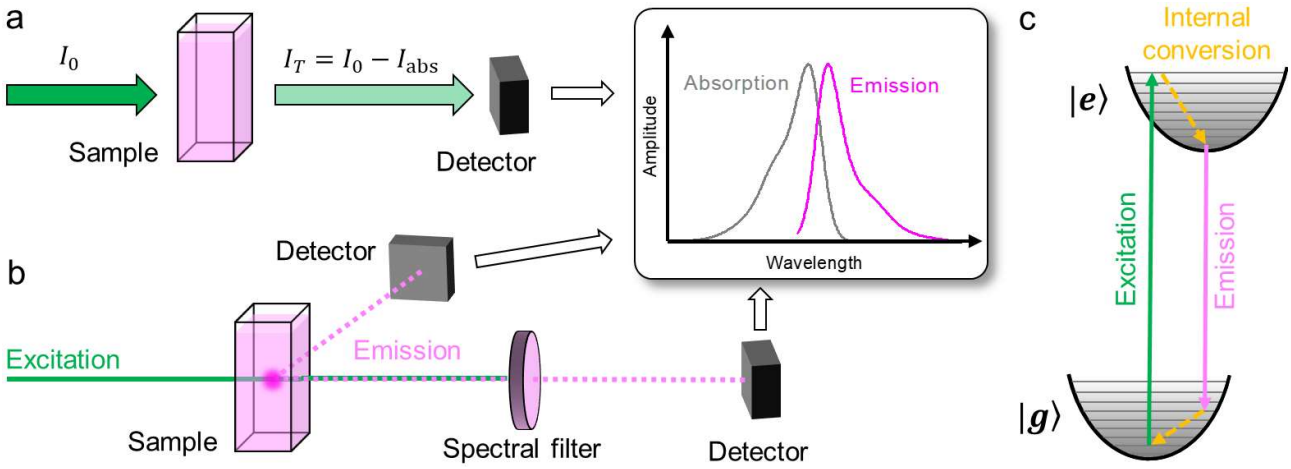

Figure 2.1. (a) Principle of absorption spectroscopy. The absorption spectrum is measured by scanning the excitation wavelength (inset). (b) Principle of PL spectroscopy. After photoexcitation (green), the PL signal can be detected isolated from the excitation source either by placing the detector in a separate direction (top path) or by adding a spectral filter to block the excitation light (bottom path), or both. The PL spectrum (inset) is measured by spectrally dispersing the PL signal in a spectrograph prior to detection. (c) Energy diagram illustrating the cycle of absorption (green arrow) reaching high-lying states in the first excited state manifold ($|e\rangle$), internal conversion (yellow dashed arrow) to the bottom states of $|e\rangle$, followed by relaxation back to the electronic ground state ($|g\rangle$) under emission of a photon, i.e., PL.

This limitation does not exist for PL spectroscopy, as it can be measured in a background-free geometry (Figure 2.1b), which greatly enhances the sensitivity of this technique. Specifically, an excitation beam continuously irradiates the sample thereby exciting a certain fraction of the molecules/systems. Subsequently, the system can spontaneously relax back to the electronic ground state under emission of a photon (i.e., PL; Figure 2.1c). In an isotropic sample with randomly oriented emitters, these photons are also emitted in a random direction and, therefore, can be collected and subsequently detected spatially separated from the excitation source (Figure 2.1b, top path). Furthermore, PL typically occurs frequency shifted with respect to the absorption spectrum by the so-called Stokes shift. Therefore, one can additionally use spectral filters to isolate the signal of interest from the excitation source (Figure 2.1b, bottom path). In PL measurements, however, special care has to be taken in order to avoid reabsorption of PL, which may alter the shape of the detected spectrum. As the PL signal has to pass through (parts of) the same sample prior to detection, photons may, thus, be reabsorbed by the sample. This is particularly important for samples with small to negligible Stokes shift, i.e., with spectrally overlapping absorption and emission bands. As the probability for reabsorption of a photon depends on the optical density of the sample, it is preferable to record PL spectra using optically thin samples with a maximum optical density on the order of $0.1-0.2$.

A major drawback of steady-state absorption and PL spectroscopy, however, is that they are lacking any temporal resolution, because the sample is continuously being illuminated and the signal continuously being measured. In other words, a defined time zero at which excited states dynamics are initiated is missing, which is why steady-state absorption and PL spectra do not permit to derive any dynamical properties directly. For that, one needs to excite the sample with short laser pulse that defines time zero at which the dynamical processes in the sample are initiated; this will be introduced in Section 2.2.

2.1.2 Linear Dichroism

Linear dichroism (LD) can be treated as an extension of linear absorption spectroscopy, which resolves the difference of the absorption for excitation light that is linearly polarized either parallel ($\mathrm{OD}_{||}$) or perpendicular ($\mathrm{OD}_{\perp}$) with respect to the orientation axis of an anisotropic sample. Because the probability for absorbing a photon depends critically on the alignment of the transition dipole moments of the sample relative to the incident electric field, LD spectra (and CD spectra as their circularly polarized equivalents) bear valuable information on the geometry of the system as well as the underlying molecular structure[2–5], which can for example be used for validating theoretical models. The reduced linear dichroism (LD_r) is computed as the difference of the optical densities for parallel and orthogonal polarized light normalized by the isotropic absorption:

$$\mathrm{LD}_r = \frac{\mathrm{OD}_{||} - \mathrm{OD}_{\perp}}{\mathrm{OD}_{\mathrm{iso}}} = \frac{\mathrm{OD}_{||} - \mathrm{OD}_{\perp}}{\frac{1}{3}\left(\mathrm{OD}_{||} + 2\,\mathrm{OD}_{\perp}\right)} \tag{2.2}$$

Compared to the ‘conventional’ linear dichroism (simply defined as the difference $\mathrm{OD}_{||} - \mathrm{OD}_{\perp}$) the reduced quantity LD_r offers the advantage that the signal amplitude is insensitive to measurement parameters such as the molar concentration or thickness of the cuvette. Hence, it can be interpreted as a pure measure of the alignment (or polarization) of the sample. The maximum and minimum amplitude of LD_r are 3 and -1.5, respectively, where $\mathrm{LD}_r = 3$ means perfect parallel alignment of the transition dipole moments with respect to the light polarization and $\mathrm{LD}_r = -1.5$ perfect

perpendicular alignment. Deviations from these may arise from non-ideal macroscopic alignment of the sample or due to partial cancellation of spectroscopically overlapping transitions, i.e., parallel and perpendicular components that mutually compensate. The case of $LD_r = 0$ is referred to as isotropic absorption.

In an isotropic sample the absorbing dipole moments are by definition randomly oriented and, thus, no preferential absorption of any polarization is observed. Therefore, macroscopic alignment of the dipole moments has to be established first, before LD spectra can be measured. For molecular nanotubes such alignment can be achieved by utilizing their extremely large aspect ratio (i.e., the ratio of length *versus* diameter) for LD measurements, as they tend to align along the flow in a liquid jet[6] or when the sample solution is pumped through a flow-cuvette[4]; schematically depicted in Figure 2.2.

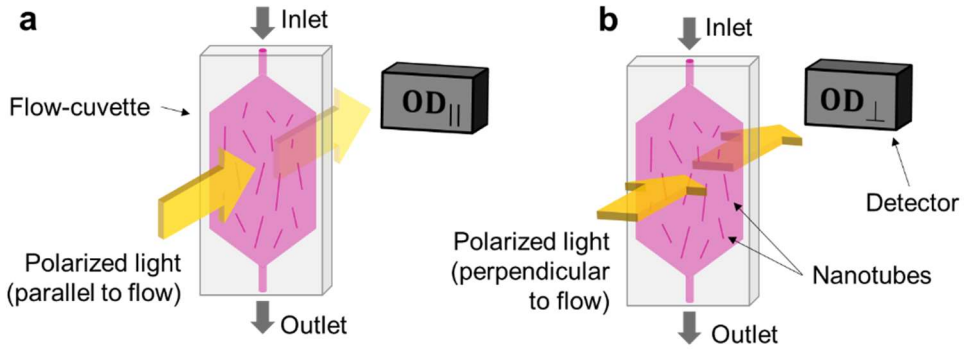

Figure 2.2. Schematic arrangement for LD measurements on molecular nanotubes for excitation light that is polarized (a) parallel and (b) perpendicular to the alignment of the nanotubes in a flow-cuvette.

Linear dichroism spectra have a direct relevance to ultrafast (time-resolved) experiments as well as microscopy experiments, as the excitation (laser) sources are polarized. Hence, any possible alignment of the sample has to be taken into account, as it may lead to preferential excitation of differently polarized excitonic transitions of the sample, e.g., Davydov split absorption bands in case of molecular aggregates (Section 1.2).

2.2 Time-Resolved Spectroscopy

Understanding the nature and timescales of the dynamical properties of a system such as the exciton transport, spectral diffusion due to (fluctuating) interactions with the surrounding environment or energy transfer between different entities in the sample requires adding the temporal dimension. In order to achieve that one can use (a train of) short laser pulses that interact with the system at a defined point of time marked by the arrival of the laser pulse at the sample and then monitor the response of the system. In this section three means of following the excited state dynamics will be introduced: (1) detecting the time-resolved PL decay, (2) adding a delayed second pulse probing the for transient changes of the sample absorption, and (3) adding a delayed third pulse to realize two-dimensional (2D) spectroscopy.

2.2.1 Time-Resolved Photoluminescence

In order to follow the PL decay in time, excited state dynamics are initiated by the absorption of a high energy photon leading to the photoexcitation of high lying vibrational or excitonic state in the first excited state manifold (see Figure 2.1c, Section 2.1.1). This initial, high energy excitation is followed by rapid intra-band relaxation to the states located at the bottom of the respective band via

internal conversion as dictated by Kasha's rule[7]. From there the system can undergo relaxation back to the electronic ground state either via a radiative channel under emission of a photon (i.e., PL) or via a non-radiative channel, i.e., the excited state energy is released into other, typically vibrational degrees of freedom (*heat*). The key difference compared to measurements conducted in the steady-state regime is the fact that instead of continuously illuminating the sample, a short laser pulse is used for the initial photoexcitation, which allows to monitor the excited state dynamics (and relaxation) thereafter.

For the purpose of measuring the PL decay on ultrafast timescales (i.e., nanoseconds down to femtoseconds) different experimental techniques are available: time-correlated single photon counting (TCSPC), PL upconversion, and streak cameras; see Ref. [8] for a complete overview. For this Thesis, the discussion will focus on streak cameras for which a schematic illustration of the experimental apparatus is shown in Figure 2.3a. The temporal resolution that can be achieved with a streak camera is typically on the order of ~10 ps, referring here to the width of the so-called instrument response function (IRF). Due to the limited response time, processes occurring on sub-picosecond timescales cannot directly be observed with a streak camera. On the positive side, time-resolved PL is a background-free measurement technique and thus excels in terms of sensitivity, which allows measuring the spectrally resolved PL decay on timescales from few picoseconds up to several nanoseconds through orders of magnitude in PL intensity (Figure 2.3b).

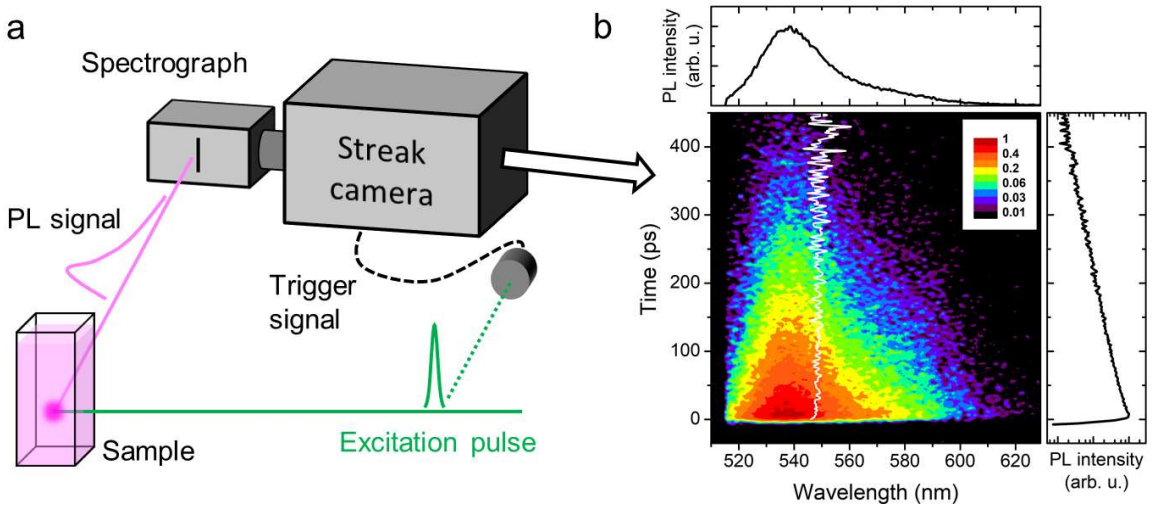

Figure 2.3. (a) Schematics of experimental apparatus for time-resolved PL measurements using a streak camera. Following excitation by a short laser pulse (green) the decay of the PL signal (magenta) is monitored as a function of time and wavelength. A fraction of the laser pulse is picked up by a photodiode and serves as a timing signal. (b) Representative PL decay map (main panel) recorded for C8S3 dissolved in methanol following excitation at ~510 nm. The PL signal was normalized to the maximum amplitude and is shown on a logarithmic color scale. The white line indicates the mean PL wavelength at each time step. The side panels show the spectral (top) and temporal (right) projections of the PL map.

For illustration, an actual PL decay map is shown in the center panel of Figure 2.3b, where the PL signal amplitude (depicted on a color scale) is spectrally and temporally resolved on the horizontal and vertical axis, respectively. The projection of the PL signal along the temporal axis yields the steady-state PL spectrum as shown in the upper panel, which can be directly compared to results from independent measurements (Section 2.1.1). Projection of the PL signal along the wavelength axis yields the temporal dependence of the PL signal denoted as PL transient (Figure 2.3b, right panel). Here, the PL signal decays exponentially with a single time constant τ following pulsed laser excitation at time-zero. In more general cases, there may be more than one time constant necessary

to fully characterize the observed dynamics, as different process in the sample occur with different rates ($\propto \tau^{-1}$). In any case, the measured PL decay of the sample is convoluted with the IRF, which is evident from the finite rise time of the signal at negative times:

$$S_{\mathrm{PL}}(\lambda, t) = \mathrm{IRF} \otimes S' = \int \mathrm{IRF}(t-\tau) S'(\lambda, t) d\tau. \tag{2.3}$$

Here, $S_{\mathrm{PL}}(\lambda, t)$ is the measured PL decay map as a function of wavelength and time, whereas $S'(\lambda, t)$ is the 'real' response of the system. Knowledge of the temporal shape of the IRF, hence, permits retrieving the PL lifetime(s) by fitting the measured transients to Eq. 2.3.

Another useful quantity that can be extracted from a PL decay map is the time-resolved mean frequency of the PL spectrum $\langle \nu(t) \rangle$ shown as a white line in Figure 2.3b. This quantity contains valuable information on energy transfer dynamics[9,10], and exciton thermalization as well as spectral diffusion[11–13]. The mean frequency is computed by cutting a horizontal slice from the PL decay map, i.e., the PL spectrum at a specific time after photoexcitation, and determine its 1st moment according to:

$$\langle \nu(t) \rangle = \frac{\int \nu \, S_{PL}(\nu, t) d\lambda}{\int S_{PL}(\nu, t) d\lambda}. \tag{2.4}$$

In the shown case the mean frequency is a constant (a vertical line) indicating a negligible degree of spectral diffusion on the timescale of the PL decay. Again, very fast modulations of $\langle \nu(t) \rangle$ cannot be resolved due to the limited temporal resolution, which thus calls for experimental techniques with an enhanced temporal resolution such as transient absorption and 2D spectroscopy.

2.2.2 Transient Absorption

Another well-established technique to track ultrafast processes of a system in its excited state is the so-called pump-probe spectroscopy. The expression 'pump-probe' refers to the sequence of laser pulses, where the first pulse *pumps* the sample and initiates excited state dynamics, which are then *probed* by a second pulse after a variable delay time T. Spectrally dispersing the broad-band probe pulse after the sample permits measuring the transient changes of the sample absorption in presence and absence of the pump pulse, for which the technique is also called transient absorption (TA) spectroscopy. Because TA spectroscopy is rather simple to implement experimentally and the data analysis is more intuitive than for other types of non-linear spectroscopies (transient grating, photon echo, 2D spectroscopy, *etc.*) it is frequently used to study excited state dynamics in various systems[14–18]. The attainable temporal resolution of this technique is on the order of $\sim$100 attoseconds[19] up to tens of femtoseconds as determined by the durations of the pump and probe pulses. In the framework of this Thesis, it is instructive to consider TA spectroscopy as a simplified predecessor for two-dimensional (2D) spectroscopy, as many of the concepts considered herein will directly translate to the next section about 2D spectroscopy.

A schematic layout for TA spectroscopy is shown in Figure 2.4a. Following the interaction of a pump pulse with the sample at $t = 0$, the probe pulse interrogates how the sample has evolved in its excited state after a certain delay time T. In practice, TA spectra are measured by modulating the repetition rate of the pump pulses: every other pump pulse is blocked, while the probe is kept at its original repetition rate. As a result, probe spectra S are recorded alternatingly with either the pump beam blocked (S_{off}) or the pump beam open (S_{on}). In a typical experiment, this is done repetitively for a number of pulses and subsequently averaged for improved signal-to-noise ratio. In analogy to

linear absorption spectroscopy, the TA signal is computed as the change of the sample transmission (ΔT) over the total transmission (T) by taking the difference of the probe spectra with the pump on versus pump off. The associated change in optical density ΔOD can be determined as follows:

$$\Delta\mathrm{OD} = -\log\left(\frac{\Delta T}{T}+1\right) = -\log\left(\frac{S_{\mathrm{on}}-S_{\mathrm{off}}}{S_{\mathrm{off}}}+1\right). \qquad (2.5)$$

In literature, there is no consensus about which quantity (ΔOD or ΔT/T) is to be preferred and different conventions may apply in different fields; in this Thesis only ΔOD will be used. The main difference concerns the mathematical sign of the TA signal, which is flipped upon applying Eq. 2.5.

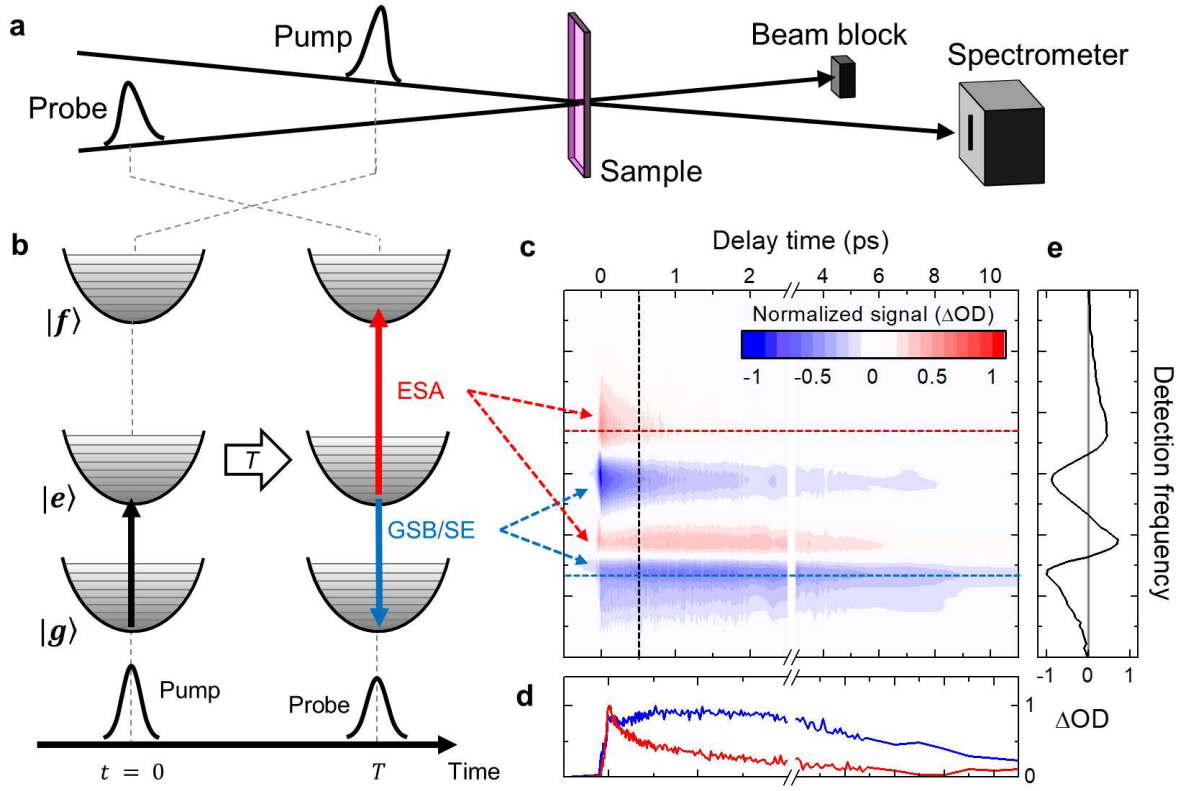

Figure 2.4. (a) Principle of transient absorption (pump-probe) spectroscopy. The pump and probe beams are spatially overlapped in a sample. The probe beam is spectrally dispersed and detected for a given delay time between pump and probe pulse. (b) Level diagram for different processes that may occur upon interaction of the time delayed probe pulse with the sample following excitation by the pump pulse. The processes of GSB/SE and ESA are shown as blue and red arrows, respectively. (c) TA map with the detection frequency on the vertical axis and delay time on the horizontal axis. The normalized change of the optical density (ΔOD) of the sample is shown on a color scale between -1 and $+1$ with increments in steps of 0.1. A negative delay time means the probe pulse arrives at the sample before the pump pulse. (d) Horizontal and (e) vertical slices of the TA map along the dashed lines (in the same colors) in panel (c) representing the TA spectrum and transients at a given delay, respectively.

In many experiments, the probe pulse is chosen to be spectrally broad (e.g., from a white-light continuum source) in order to cover all relevant absorption bands (i.e., optical transitions) of the sample under study. In contrast, the pump pulse spectrum can be made spectrally narrow in order to exclusively excite a single or a small sub-set of absorption bands of the sample. Such spectral selectivity can be advantageous in order to study for example energy transfer between two species (A and B) by only optically exciting species A with a narrow-band pump pulse and then monitor the response of both species using the broad-band probe pulse. Alternatively, making the pump pulse spectrally broad to simultaneously excite multiple absorption bands may allow the observation of oscillatory components in the TA signal[18,20].

In theory, three different types of interaction between the probe pulse and the sample in its excited state can be distinguished: ground-state bleach, stimulated emission and excited state absorption (Figure 2.4b). Ground-state bleach (GSB) occurs as the probe pulse encounters a decreased fraction of molecules/systems in the sample residing in the electronic ground state for which optical excitation could have occurred in absence of the pump pulse. As a result, this transition ($|g\rangle \rightarrow |e\rangle$) is less likely to occur after interaction with the pump pulse than without and, thus, appears *bleached*. Note that in the case of multiple absorption bands of the sample, GSB affects all bands that share a common electronic ground-state. The second type of TA signal is stimulated emission (SE), where interaction with the probe pulse leads to the de-excitation ($|e\rangle \rightarrow |g\rangle$) of the sample under emission of a photon – similar to the working principle of a laser. The third type of TA signal is excited-state absorption (ESA), which is a new absorption channel reaching from the first electronic excited state to even higher excited states, i.e., $|e\rangle \rightarrow |f\rangle$. The associated changes in optical density (ΔOD) of the sample can either be negative ('*more light is transmitted*') as is the case for GSB and SE or positive ('*less light is transmitted*') as is the case for ESA. As an example, an actual TA map recorded for molecular nanotubes is shown in Figure 2.4c, where blue (negative) and red (positive) features correspond to GSB/SE and ESA signals, respectively.

From such a TA map the characteristic time constants can be extracted by taking a horizontal slice, which yields the temporal dependence (transients) of the chosen GSB/SE or ESA feature (Figure 2.4d). Meanwhile, a vertical slice yields the TA spectrum at a given delay time (Figure 2.4e) showing contributions from both GSB/SE and ESA. Unfortunately, from a single measurement such a slice does not permit to extract the dependence of the TA signal on the excitation frequency and, thus, deconvolute different GSB/SE and ESA contributions occurring at different excitation frequencies. Although this can be accomplished by performing a set of TA measurements at different excitation narrow-bandwidth wavelengths, the experimenter will face the so-called time-bandwidth problem: a short light pulse requires broad spectral bandwidth and, thus, compromises the spectral selectivity of the experiment and *vice versa*. Two-dimensional (2D) spectroscopy can remedy this limitation.

2.2.3 Two-Dimensional (2D) Spectroscopy

Two-dimensional (2D) spectroscopy belongs to the family of non-linear spectroscopies and is the successor of photon echo spectroscopy, which has first been demonstrated in 1964[21]. Substantial progress in further developing the technique and applying it to molecular systems has been achieved during the 1980s by A. M. Weiner and co-workers[22] as well as during the 1990s at the University of Groningen by D. Wiersma and co-workers[23]. Photon echo spectroscopy is a powerful technique, which utilizes a sequence of ultrashort laser pulses to extract information on the magnitude and timescale of solute-solvent interactions in the condensed phase[24].

In principle, 2D spectroscopy contains the same information as photon-echo spectroscopy as it measures the third-order polarization induced in a material by the sequential interaction with three (or more) laser pulses. The main difference is that instead of excitation and detection *time* coordinates (as in photon echo), the information is spread along the excitation and detection *frequency* axes onto a two-dimensional map, thus, earning it the name 2D spectroscopy. This representation allows to directly draw correlations between the two frequencies and grants access to peak shapes and cross peaks, which cannot be directly probed using conventional TA spectroscopy. Therefore, 2D spectroscopy is best known for its capabilities to discern inhomogeneous from homogenous line

broadening[25–27], resolve coupling between different electronic transitions as well as energy transfer and detect coherences involved therein[6,28–30], or to directly probe exciton-exciton interactions[31–36].

Over the past decades, numerous experimental implementations for 2D spectroscopy have been devised, which now cover a substantial region of the electromagnetic spectrum ranging from terahertz (THz) over infrared (IR) to the NIR/visible and further into the (near)UV; the details can be found in numerous reviews[37–39]. The analysis and interpretation of 2D spectra is most commonly performed in the framework of the perturbation theory of the density matrix and non-linear response function theory; comprehensive descriptions are offered in literature[40–42]. The discussion presented in this section aims to provide a more general and intuitive picture of 2D spectroscopy and, thus, focusses on the essential concepts. More quantitative descriptions will be provided in Chapter 3 and 5.

For a general understanding of 2D spectroscopy it is instructive to consider it as an extension of TA spectroscopy with the salient difference that instead of a single pump pulse, the sample is excited by a pair of two collinear pump pulses with an adjustable delay τ (called coherence time); schematically depicted in Figure 2.5a and b. As in TA spectroscopy, the probe pulse is delayed with respect to the second pump pulse by the waiting time T. Note that this particular beam geometry is referred to as pump-probe geometry; other beam geometries used for 2D spectroscopy are discussed in Ref. [37].

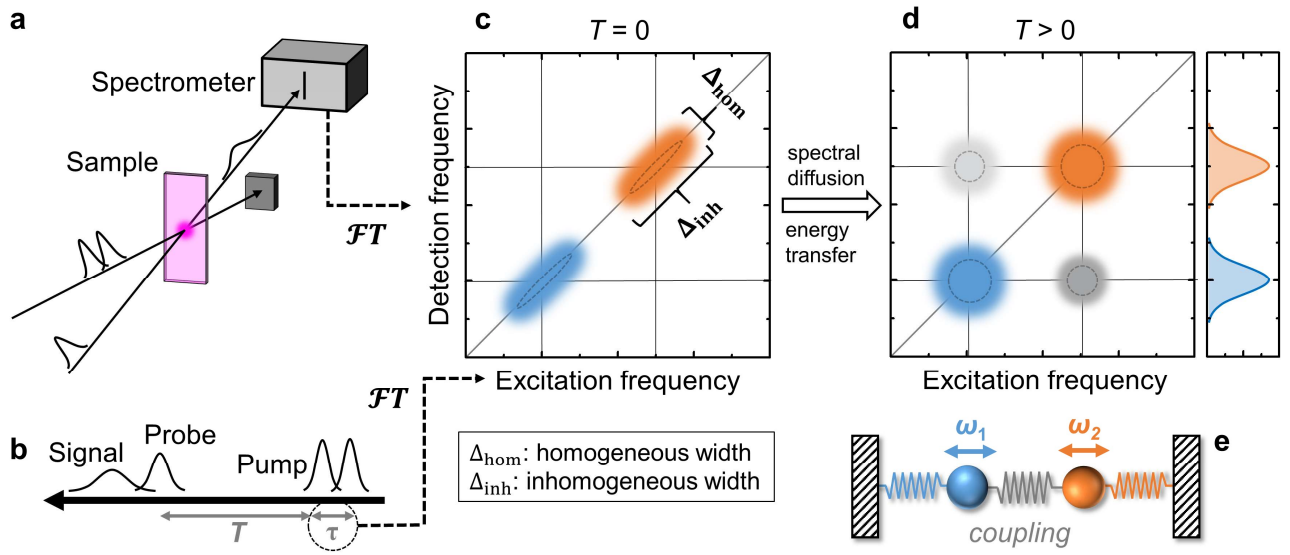

Figure 2.5. (a) Principle of 2D spectroscopy in a pump-probe arrangement: A pump pulse pair with an adjustable time delay τ (i.e., the coherence time) and a probe pulse delayed by the waiting time T are spatially overlapped in the sample. The third-order signal is emitted in the same phase-matched direction as the probe beam, heterodyned with the probe field and spectrally resolved in a spectrograph, which provides the detection frequency axis of the 2D spectra. (b) Pulse sequence for 2D spectroscopy. The excitation axis of the 2D spectra is constructed via Fourier transformation with respect to the coherence time τ. (c) and (d) Artist impression of 2D spectra measured for waiting times of $T = 0$ and $T > 0$, respectively. The spectra comprise two diagonal peaks (orange and blue) at different resonance frequencies as well as the corresponding cross peaks (gray) in panel (d). Diagonal lines are drawn for $\omega_{\mathrm{excitation}} = \omega_{\mathrm{detection}}$. In panel (c) the peak widths along the diagonal and anti-diagonal lines are denoted as Δ_{inh} (inhomogeneous linewidth) and Δ_{hom} (homogeneous linewidth), respectively. During the waiting time T between panel (c) and panel (d) energy transfer and spectral diffusion may occur leading to the shown peak pattern. The side panel shows the projection of the 2D spectrum along the excitation axis. (e) Schematic illustration of two oscillators (blue and orange) with resonance frequencies of ω_1 and ω_2, which in this picture are determined by the respective spring constant. In 2D spectra of such a system, off-diagonal cross peaks would only be observed if the oscillators are coupled via e.g. a third spring (gray); under the assumption of an anharmonic potential.

In analogy to TA spectroscopy, the detection axis of a 2D spectrum (Figure 2.5c and d) is readily obtained by detection of the spectrum of the signal field heterodyned with the probe field. The latter is equivalent to a Fourier transformation, as the signal field in the time domain is translated into the frequency domain, i.e., the spectrum. The excitation axis can be constructed by controlling the relative delay τ between the two pump pulses. Depending on the pulse separation τ, the pump pulses then interfere in the sample thereby creating a fringe pattern of the spectral intensity:

$$I_{\mathrm{pump}}(\omega) = 2\, I_{\mathrm{pulse}}(\omega)\, [1 + \cos(\omega\tau)]. \tag{2.6}$$

Here, $I_{\mathrm{pulse}}(\omega)$ is the spectral intensity of the pump pulses. By systematically scanning τ, the pump spectrum and, thus, also the signal at a given frequency are periodically modulated (due to the cosine term in Eq. 2.6). Fourier transformation with respect to τ then retrieves the excitation axis and relates the periodical appearance and disappearance of the signal to the modulation of the pump spectrum at a given frequency. From a different perspective, one may therefore think of a 2D spectrum as a collection of many TA spectra (or slices) stitched together along the excitation axis. In practice, different strategies exist to generate two time delayed pump pulses, e.g., beam-splitters and mechanical delay lines[43], pairs of birefringent glass wedges[44,45], or pulse shapers[46,47].

As the final step, one faces the task to isolate the desired signal from all other unwanted contributions. In the beam geometry presented in Figure 2.5a, the spectrometer also detects pump-probe signals due to the interaction of either of the pump pulses with the sample (as discussed in the preceding section) as well as free induction decay due to interaction with any of the (pump or probe) pulses. An elegant way to isolate the desired signal relies on so-called phase cycling, where the phase difference ($\Delta\phi_{12}$) of the two pump pulses is changed between two consecutive laser shots. In fact, the third-order signal is sensitive to $\Delta\phi_{12}$, whereas the unwanted signals are not. By changing (or cycling) from $\Delta\phi_{12} = 0$ to $\Delta\phi_{12} = \pi$ the sign of the third-order signal flips, which means it does not cancel by computing the difference of both spectra, i.e., $S = S_{\Delta\phi_{12}=0} - S_{\Delta\phi_{12}=\pi}$. This results in the final 2D spectra that are schematically depicted in Figure 2.5c and d for different waiting times, i.e., different delays between the pump and probe pulses.

At zero waiting time (Figure 2.5c) the diagonal peaks in the 2D spectra may appear elongated along the diagonal line (at $\omega_{\mathrm{exc}} = \omega_{\mathrm{det}}$), which directly reveals the inhomogeneous (Δ_{inh}) and homogeneous (Δ_{hom}) contributions to the absorption spectrum. This elongation occurs because the emitters have virtually no time to interact with the fluctuating environment and, therefore, retain the memory of the excitation frequency. As time progresses, i.e., during the waiting time T, the frequency memory is *washed out* due to spectral diffusion (or dephasing). Specifically, spectral diffusion means that the transition frequency of an emitter changes over time due to interactions with the dynamically fluctuating environment until it has eventually sampled the entire inhomogeneous width of the sample. As a result, the diagonal peaks become increasingly circular (Figure 2.5d). The timescale(s) of the fluctuations can readily be accessed by evaluating the peak shape in the 2D spectra at different waiting times. A more quantitative description of spectral diffusion will be presented in Chapter 3.

Meanwhile, coupling between different electronic transitions and energy transfer are evident from the formation of the so-called cross peaks, for which the detection frequency is different than the excitation frequency, i.e., $\omega_{\mathrm{detection}} \neq \omega_{\mathrm{excitation}}$. For a conceptual understanding of how electronic coupling leads to the formation of cross peaks, one can consider two uncoupled spring oscillators (1 and 2) with eigenfrequencies ω_1 and ω_2 (Figure 2.5e), where $\omega_1 \neq \omega_2$ for the sake of argument; see

also Ref. [48]. Resonant excitation of such an oscillator, e.g., with a light field, induces oscillations at the respective eigenfrequency. In absence of any damping, the oscillator continues to oscillate at its eigenfrequency, until it is detected after a certain time giving rise to a signal at the same detection frequency $\omega_{\text{detection}} = \omega_{\text{excitation}}$, i.e., a diagonal peak (as shown in Figure 2.5c). After coupling these two oscillators, e.g., by connecting them with an additional spring, excitation of one the oscillators will ultimately cause the other oscillator to start moving as well at its eigenfrequency (assuming that the coupling is weak enough to not alter their original eigenfrequencies). In other words, energy transfer from oscillator 2 (after excitation at ω_2) to oscillator 1 can be detected at the resonance frequency of the latter ω_1, which is encoded in the respective cross peak (Figure 2.5d, gray). A more detailed account on the formation of cross peaks will be presented in Chapter 5.

Hitherto, all considerations have been presented under the assumption that during a spectroscopic experiment one exciton evolves independently from all other excitons. Strictly speaking, this only holds for sufficiently low excitation intensities. Under intense laser radiation, excitons are known to mutually interact, for example via exciton-exciton annihilation, as was introduced in Section 1.3.1. Formally, exciton-exciton interactions (EEI) can be described by fifth-order non-linear processes, as their occurrence requires excitation of (at least) two excitons. Such a fifth-order extension to the 'conventional' third-order 2D spectroscopy was introduced recently[31,33,35,49]. The EEI signal occurs at twice the excitation frequency of a single exciton, i.e., at 2ω. In conventional third-order spectroscopy the occurrence of EEI is only observed as a perturbation of the one-exciton dynamics. In contrast, by using fifth-order 2D spectroscopy it is possible to directly measure the EEI dynamics (i.e., spectrally isolated from the one-exciton signal), which bear valuable information on the exciton delocalization and exciton diffusion. More details on the experimental implementation and theoretical background of EEI2D spectroscopy will be provided in Chapter 5.

2.3 Microfluidics

Microfluidics is the field of controlling, manipulating and monitoring streams of fluids or gases in a network of channels with sizes on the order of 10s up to 100s of micrometer[50]. The roots of this field range back to 1979, when the first miniaturized microfluidic device for analytical applications was demonstrated by Terry *et al.*[51]. Such miniaturization allows to combine several stages of the aforementioned functionalities in a single 'device', which is often condensed in the term 'lab-on-a-chip'. In recent years, microfluidics has experienced a surge in interest throughout various disciplines owing to its high degree of adaptability, since flowcells can be manufactured relatively inexpensive and tailored towards specific applications in e.g. biomedicine and drug discovery[52], synthetic chemistry[52,53], and as analytical tools[54].

In many realizations, microfluidics utilizes the fact that confinement of fluids in microscale volumes fundamentally changes their behavior. In fact, in microfluidics the dynamics of fluids are generally characterized by low Reynoldsnumbers ($\text{Re} < 10^3$) leading to laminar rather than turbulent flows, which occur at large Reynoldsnumbers ($\text{Re} > 10^3$)[55]. Hence, mixing of two reactants occurs predominantly via slow diffusion across the interface, which opens unprecedented opportunities for synthetic chemistry, as the mixing rates of reactants can be balanced to their reaction rate in real time[56]. In some applications, however, rapid mixing of two reactants is required for which laminar flow is a limitation rather than an advantage. This has led to the development of a droplet microfluidics[57,58] and a range of micromixers that allow efficient mixing of two or more chemicals as

fast as several milliseconds. Along the same lines, microfluidics have also increasingly been used as a powerful tool to control self-assembly and steer the final species towards otherwise unfavorable configurations[59–61].

Interfacing microfluidics with optics[62] in general and (time-resolved) optical spectroscopy in particular is a powerful combination as it bridges the gap between chemical or structural modifications of the sample on microsecond to minutes timescales and femto- to picoseconds excited state dynamics accessible with ultrafast spectroscopy. In that context, various modes of detection have been explored including FTIR absorption[63,64], steady-state[65] time-resolved PL[66,67], transient absorption and 2D spectroscopy[34,68] as well as X-ray scattering[69] as notable examples. At the same time, microfluidics reduces the sample amount that is required for an experiment to a minimum but still maintaining the sample refreshment, which is crucial for many biological applications where only small sample quantities might be available[70,71].

In Chapter 4 and 5, microfluidics will be used to obtain spectroscopic access to non-equilibrium and, thus, short-lived intermediate species of molecular nanotubes. In fact, the supramolecular structure of self-assembled molecular aggregates is known to sensitively respond to changes of the molar concentration of the aggregating dye molecules, the addition of surfactants[72,73], and/or composition of the solvent[74,75]. In principle, any of these effects can be exploited in microfluidics, which allows to introduce the mentioned changes in a controlled environment and subsequently monitor the response of the system in real time.

2.4 Single-Aggregate Microscopy

Since the pioneering work of Antonie van Leeuwenhoek on optical microscopy in the 17th century[76], which he used to study biological samples and crystals, microscopy has progressively been pushed towards imaging extremely faint samples and resolving smaller and smaller structures. Concerning the former, breakthrough results were achieved by Frits Zernike who invented the so-called phase-contrast microscope that could be used for imaging of otherwise completely transparent samples. For his achievements Zernike was awarded the Nobel Prize in Physics in 1953[77]. Another notable milestone in the field was reached, when Moerner *et al.*[78] and Orrit *et al.*[79] demonstrated that it is feasible to perform spectroscopic experiments on a single molecule immobilized on a substrate. The striking advantage of single-molecule spectroscopy – or in more general terms single-'object' spectroscopy – is its capability to overcome ensemble-averaging[80].

In spectroscopy, ensemble averaging means that the properties and dynamics of one single emitter are *washed out* by spectrally overlapping and temporally asynchronous signals from many other emitters that are simultaneously detected in a conventional experiment. In other words, experiments on bulk samples containing a large number of emitters effectively measure a mean value of a spectroscopic observable that is representative of the whole ensemble. For example, in a typical transient absorption experiment there are 10^{10} molecules in the focal volume (volume $V \sim 1.6$ nL, molar concentration $c = 10^{-4}$ M) all giving rise to slightly different signals, as each individual molecule 'feels' a slightly different surrounding. These different contributions are averaged upon detection, which makes it impossible to decipher spectral diffusion due to the interaction of a single emitter with its local, dynamically fluctuating environment or (in the case of structurally more complex systems) to discern structural heterogeneity of the sample from inhomogeneity that is inherent to one single object (static disorder)[81]. Yet, such insight is highly desirable to understand the

timescale and magnitude of heterogeneities in the energetic landscape that dictate the photophysical properties of a system. Single-object microscopy and spectroscopy is able to overcome this limitation by measuring one emitter at a time and, thus, construct the distribution of parameters rather than measuring its weighted mean value. As a few notable examples, single object microscopy and spectroscopy has successfully been applied to extract the static disorder in J-aggregates[82,83], measure the Stokes shift of a single molecule[84], resolve molecular orientations within natural[85,86] and artificial light harvesting antennae[87] via polarization resolved excitation spectroscopy, study quenching states in photosynthetic bacteria[88] and directly image the transport of excitation energy through nanofibres[89–92].

Studying individual objects with characteristic sizes of several nanometers using optical microscopy reaches limits of what is physically achievable: the diffraction limit. The latter was originally formulated by Ernst Abbe in 1873 and describes the minimum distance Δr between two point sources of light that can still be distinguished upon imaging[93]:

$$\Delta r \approx 0.61 \frac{\lambda}{\mathrm{NA}} \tag{2.7}$$

Hence, it is the light wavelength λ and the numerical aperture ($\mathrm{NA} = n \sin(\theta)$; n refractive index, θ collection angle of the PL signal) of the imaging system that determine the resolution limit of the microscope[94]. The reason for this limitation is the fact that each point source is imaged onto its so-called point spread function (PSF; typically approximated as a Gaussian function), which literally describes the spread of a point source in its image. For two individual objects that are sufficiently close in the sample plane, their PSFs start to overlap and eventually merge in the image plane, which renders them indistinguishable from a single object. The consequence of this resolution limit can easily be experimentally visualized by imaging an object that is much smaller than the size of the point spread function (e.g., photoluminescent nanobeads; Figure 2.6a), where the imaged PL intensity distribution is significantly wider than the object itself (Figure 2.6b). In that regard, molecular nanotubes present an interesting case: in one dimension they act as point sources due to their small diameter of only ~10 nm, while in the other dimension they are essentially a 'continuous film' due to their extended length.

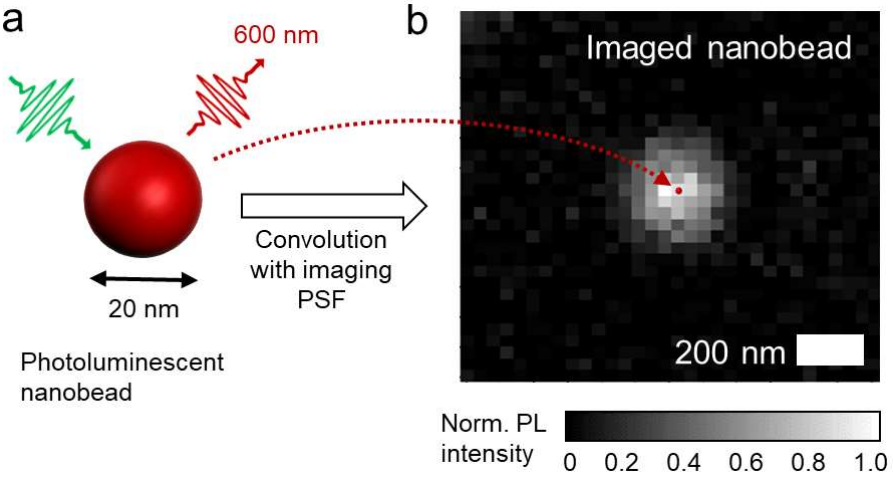

Figure 2.6. (a) Schematic representation of a photoluminescent nanobead with a diameter of 20 nm. (b) Experimentally obtained microscope image of a photoluminescent nanobead; the actual size of the nanobead is indicated by the red dot. The image is broader due to convolution with the imaging PSF.

2.5 Cryo-TEM

Since one half the 1986 Physics Nobel Prize was awarded to Ernst Ruska "for his fundamental work in electron optics, and for the design of the first electron microscope"[95], transmission electron microscopy (TEM) has evolved to the work horse characterization technique in material sciences. TEM works as an analogue to conventional light microscopy with the salient difference that it uses highly accelerated electrons (with several keV of energy) rather than photons to generate an image[96]. The advantage of using highly accelerated electrons is that the de Broglie wavelength of the electrons is on the order of $\lambda_{\mathrm{el}} \approx h\left(\sqrt{2m_e eV}\right)^{-1} \approx 2.5$ pm assuming an acceleration voltage of 200 kV. The theoretical resolution limit of optical microscopy is thereby surpassed by orders of magnitude (see Eq. 2.7). In reality, the attainable resolution is lower than 2.5 pm due to other limiting factors such as spherical aberrations, but still atomic resolution (~1 Å) is nowadays almost routinely achieved.

In parallel, cryogenic transmission electron microscopy (cryo-TEM) has increasingly been applied to biological and other 'soft' systems such as protein complexes[97], bacterial light harvesting antennae[98] or molecular aggregates[99,100]. By *shock*-freezing these systems it was possible to study them in their native, typically aqueous environment and enabled three-dimensional model reconstructions of the underlying structures with atomic resolution[101]. These developments culminated in the 2017 Nobel Prize in Chemistry being jointly awarded to Jacques Dubochet, Joachim Frank and Richard Henderson "for developing cryo-electron microscopy for the high-resolution structure determination of biomolecules in solution"[102].

One of the major challenges that had to be overcome for high quality cryo-TEM images of organic (soft) systems is their susceptibility to photoinduced damage caused by inelastic scattering of highly accelerated electrons impinging on the sample[103–105]. Therefore, it is important to minimize the electron radiation dose of the samples. Using a lower dose for imaging, however, also reduces the attainable contrast, which is already low for biological samples as they hardly contain any heavy elements that would give rise to scattering contrast. Therefore, one has to resort to using so-called phase-contrast for imaging, which can be optimized for specific spatial frequencies in the image by tuning the contrast transfer function (CTF) via defocusing. Note that phase-contrast in electron microscopy works analogously to phase-contrast in optical microscopy, which was discovered by Frits Zernike. However, a rigorous and complete account of image formation in transmission electron microscopy is beyond the scope this Thesis and can be found in literature[96].

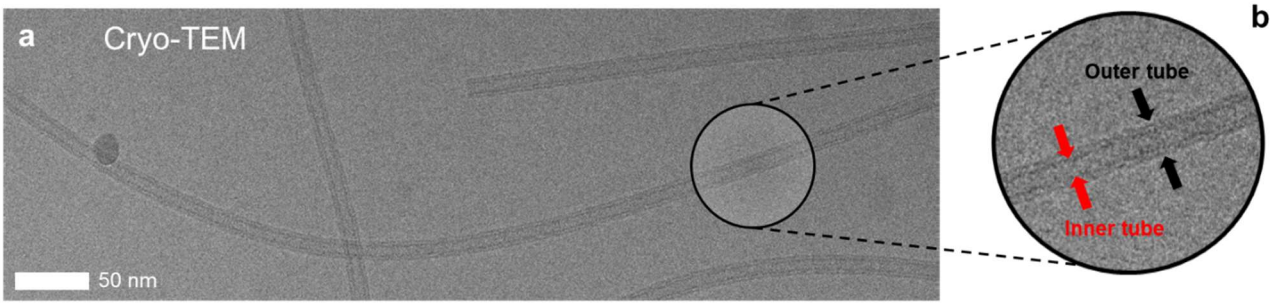

Figure 2.7. (a) Representative cryo-TEM micrograph of molecular nanotubes. (b) Enhanced view of the double-walled structure of the shown nanotubes. The contours of the inner (red arrows) and outer tube (black arrows) can readily be distinguished in the raw image.

An example of cryo-TEM imaging is shown in Figure 2.7a for molecular nanotubes based on C8S3. The double-walled geometry of these nanotubes can readily be distinguished in the raw image and allows extraction of the characteristic sizes such as inner and outer diameter (Figure 2.7b). In this Thesis, cryo-TEM will be used for the structural characterization of the molecular nanotubes, which is not possible with conventional light microscopy. In fact, cryo-TEM has been proven particularly useful working hand in hand with (ultrafast) spectroscopy[48,106,107], exciton theory/spectral calculations[5,106,108,109] and molecular dynamics (MD) simulations[110–112] by providing constraints on the characteristic sizes and geometry of the studied system.

2.6 References

1. Hollas, J. M. *Modern Spectroscopy*. (John Wiley & Sons, 2004).
2. Norden, B.; Kubista, M.; Kurucsev, T. Linear dichroism spectroscopy of nucleic acids. *Q. Rev. Biophys.* **25,** 51–170 (1992).
3. Didraga, C.; Klugkist, J. A.; Knoester, J. Optical Properties of Helical Cylindrical Molecular Aggregates: The Homogeneous Limit. *J. Phys. Chem. B* **106,** 11474 (2002).
4. Clark, K. A.; Cone, C. W.; Vanden Bout, D. A. Quantifying the Polarization of Exciton Transitions in Double-Walled Nanotubular J-Aggregates. *J. Phys. Chem. C* **117,** 26473–26481 (2013).
5. Friedl, C.; Renger, T.; von Berlepsch, H.; Ludwig, K.; Schmidt am Busch, M.; Megow, J. Structure Prediction of Self-Assembled Dye Aggregates from Cryogenic Transmission Electron Microscopy, Molecular Mechanics, and Theory of Optical Spectra. *J. Phys. Chem. C* **120,** 19416–19433 (2016).
6. Sperling, J.; Nemeth, A.; Hauer, J.; Abramavicius, D.; Mukamel, S.; Kauffmann, H. F.; Milota, F. Excitons and disorder in molecular nanotubes: a 2D electronic spectroscopy study and first comparison to a microscopic model. *J. Phys. Chem. A* **114,** 8179–8189 (2010).
7. Kasha, M. Characterization of Electronic Transitions in Complex Molecules. *Discuss. Faraday Soc.* **9,** 14–19 (1950).
8. Lakowicz, J. R. *Principles of fluorescence spectroscopy*. (Springer, 2006).
9. Kagan, C. R.; Murray, C. B.; Bawendi, M. G. Long-range resonance transfer of electronic excitations in close-packed CdSe quantum-dot solids. *Phys. Rev. B* **54,** 8633–8643 (1996).
10. Crooker, S. A.; Hollingsworth, J. A.; Tretiak, S.; Klimov, V. I. Spectrally Resolved Dynamics of Energy Transfer in Quantum-Dot Assemblies: Towards Engineered Energy Flows in Artificial Materials. *Phys. Rev. Lett.* **89,** 186802 (2002).
11. Pugžlys, A.; Augulis, R.; Van Loosdrecht, P. H. M.; Didraga, C.; Malyshev, V. A.; Knoester, J. Temperature-dependent relaxation of excitons in tubular molecular aggregates: fluorescence decay and Stokes shift. *J. Phys. Chem. B* **110,** 20268–20276 (2006).
12. Conyard, J.; Addison, K.; Heisler, I. A.; Cnossen, A.; Browne, W. R.; Feringa, B. L.; Meech, S. R. Ultrafast dynamics in the power stroke of a molecular rotary motor. *Nat. Chem.* **4,** 547–551 (2012).
13. Akselrod, G. M.; Prins, F.; Poulikakos, L. V.; Lee, E. M. Y.; Weidman, M. C.; Mork, A. J.; Willard, A. P.; Bulović, V.; Tisdale, W. A. Subdiffusive exciton transport in quantum dot solids. *Nano Lett.* **14,** 3556–3562 (2014).
14. Wilson, K. S.; Wong, C. Y. In Situ Measurement of Exciton Dynamics during Thin-Film Formation Using Single-Shot Transient Absorption. *J. Phys. Chem. A* **122,** 6438–6444 (2018).
15. Engel, E.; Leo, K.; Hoffmann, M. Ultrafast relaxation and exciton–exciton annihilation in PTCDA thin films at high excitation densities. *Chem. Phys.* **325,** 170–177 (2006).
16. Maiuri, M.; Ostroumov, E. E.; Saer, R. G.; Blankenship, R. E.; Scholes, G. D. Coherent wavepackets in the Fenna-Matthews-Olson complex are robust to excitonic-structure perturbations caused by mutagenesis. *Nat. Chem.* **10,** 177–183 (2018).
17. Augulis, R.; Pugzlys, A.; van Loosdrecht, P. H. M. Exciton dynamics in molecular aggregates. *Phys. status solidi* **3,** 3400–3403 (2006).
18. Pandya, R.; Chen, R.; Cheminal, A.; Thomas, T. H.; Thampi, A.; Tanoh, A.; Richter, J. M.; Shivanna, R.; Deschler, F.; Schnedermann, C.; *et al.* Observation of Vibronic Coupling Mediated Energy Transfer in Light-Harvesting Nanotubes Stabilized in a Solid-State Matrix. *J. Phys. Chem. Lett.* **9,** 5604–5611 (2018).
19. Galli, M.; Wanie, V.; Maansson, E. P.; Trabattoni, A.; Légaré, F.; Frassetto, F.; Poletto, L.; Nisoli, M.; Calegari, F. A beamline for attosecond UV pump - XUV probe experiments. *EPJ Web Conf.* **205,** 2017 (2019).
20. Savikhin, S.; Buck, D. R.; Struve, W. S. Oscillating anisotropies in a bacteriochlorophyll protein: Evidence for quantum beating between exciton levels. *Chem. Phys.* **223,** 303–312 (1997).
21. Kurnit, N. A.; Abella, I. D.; Hartmann, S. R. Observation of a Photon Echo. *Phys. Rev. Lett.* **13,** 567–568 (1964).
22. Weiner, A. M.; Silvestri, S. De; Ippen, E. P. Three-pulse scattering for femtosecond dephasing studies: theory

and experiment. *J. Opt. Soc. Am. B* **2,** 654–662 (1985).
23. de Boeij, W. P.; Pshenichnikov, M. S.; Wiersma, D. A. Ultrafast Solvation Dynamics Explored By Femtosecond Photon Echo Spectroscopies. *Annu. Rev. Phys. Chem.* **49,** 99–123 (1998).
24. Fleming, G. R.; Cho, M. Chromophore-solvent dynamics. *Annu. Rev. Phys. Chem.* **47,** 109–134 (1996).
25. Gallagher Faeder, S. M.; Jonas, D. M.; M. Gallagher Faeder, S.; Jonas, D. M. Two-dimensional electronic correlation and relaxation spectra: Theory and model calculations. *J. Phys. Chem. A* **103,** 10489–10505 (1999).
26. Lazonder, K.; Pshenichnikov, M. S.; Wiersma, D. A. Easy interpretation of optical two-dimensional correlation spectra. *Opt. Lett.* **31,** 3354 (2006).
27. Stiopkin, I.; Brixner, T.; Yang, M.; Fleming, G. R. Heterogeneous Exciton Dynamics Revealed by Two-Dimensional Optical Spectroscopy. *J. Phys. Chem. B* **110,** 20032–20037 (2006).
28. Abramavicius, D.; Nemeth, A.; Milota, F.; Sperling, J.; Mukamel, S.; Kauffmann, H. F. Weak exciton scattering in molecular nanotubes revealed by double-quantum two-dimensional electronic spectroscopy. *Phys. Rev. Lett.* **108,** 67401 (2012).
29. Milota, F.; Prokhorenko, V. I.; Mancal, T.; von Berlepsch, H.; Bixner, O.; Kauffmann, H. F.; Hauer, J. Vibronic and vibrational coherences in two-dimensional electronic spectra of supramolecular J-aggregates. *J. Phys. Chem. A* **117,** 6007–6014 (2013).
30. Womick, J. M.; Miller, S. A.; Moran, A. M. Probing the Dynamics of Intraband Electronic Coherences in Cylindrical Molecular Aggregates. *J. Phys. Chem. A* **113,** 6587–6598 (2009).
31. Brüggemann, B.; Pullerits, T. Nonperturbative modeling of fifth-order coherent multidimensional spectroscopy in light harvesting antennas. *New J. Phys.* **13,** 025024 (2011).
32. Zhang, Z.; Wells, K. L.; Seidel, M. T.; Tan, H.-S. Fifth-Order Three-Dimensional Electronic Spectroscopy Using a Pump–Probe Configuration. *J. Phys. Chem. B* **117,** 15369–15385 (2013).
33. Dostál, J.; Fennel, F.; Koch, F.; Herbst, S.; Würthner, F.; Brixner, T. Direct observation of exciton–exciton interactions. *Nat. Commun.* **9,** 2466 (2018).
34. Kriete, B.; Lüttig, J.; Kunsel, T.; Malý, P.; Jansen, T. L. C.; Knoester, J.; Brixner, T.; Pshenichnikov, M. S. Interplay between structural hierarchy and exciton diffusion in artificial light harvesting. *Nat. Commun.* **10,** 4615 (2019).
35. Heshmatpour, C.; Hauer, J.; Šanda, F. Interplay of exciton annihilation and transport in fifth order electronic spectroscopy. *Chem. Phys.* **528,** 110433 (2019).
36. Malevich, P.; Heshmatpour, C.; Lincoln, C. N.; Ceymann, H.; Schreck, M. H.; Hauer, J. Ultrafast bi-excitonic dynamics and annihilation in molecular and mesoscopic systems. *EPJ Web Conf.* **205,** 06013 (2019).
37. Fuller, F. D.; Ogilvie, J. P. Experimental Implementations of Two-Dimensional Fourier Transform Electronic Spectroscopy. *Annu. Rev. Phys. Chem.* **66,** 667–690 (2015).
38. Nuernberger, P.; Ruetzel, S.; Brixner, T. Multidimensional Electronic Spectroscopy of Photochemical Reactions. *Angew. Chemie Int. Ed.* **54,** 11368–11386 (2015).
39. Wright, J. C. Analytical chemistry, multidimensional spectral signatures, and the future of coherent multidimensional spectroscopy. *Chem. Phys. Lett.* **662,** 1–13 (2016).
40. Mukamel, S. *Principles of Nonlinear Optical Spectroscopy*. (Oxford University Press, 1995).
41. Hamm, P.; Zanni, M. *Concepts and Methods of 2D Infrared Spectroscopy*. (Cambridge University Press, 2011).
42. Boyd, R. W. *Nonlinear Optics*. (Academic Press, 2008).
43. Son, M.; Mosquera-Vázquez, S.; Schlau-Cohen, G. S. Ultrabroadband 2D electronic spectroscopy with high-speed, shot-to-shot detection. *Opt. Express* **25,** 18950 (2017).
44. Mehlenbacher, R. D.; McDonough, T. J.; Grechko, M.; Wu, M.-Y.; Arnold, M. S.; Zanni, M. T. Energy transfer pathways in semiconducting carbon nanotubes revealed using two-dimensional white-light spectroscopy. *Nat. Commun.* **6,** 6732 (2015).
45. Lüer, L.; Rajendran, S. K.; Stoll, T.; Ganzer, L.; Réhault, J.; Coles, D. M.; Lidzey, D. G.; Virgili, T.; Cerullo, G. Lévy Defects in Matrix-Immobilized J Aggregates: Tracing Intra-and Inter-Segmental Exciton Relaxation. *J. Phys. Chem. Lett.* **8,** 547–552 (2017).
46. Grumstrup, E. M.; Shim, S.-H.; Montgomery, M. A.; Damrauer, N. H.; Zanni, M. T. Facile collection of two-dimensional electronic spectra using femtosecond pulse-shaping technology. *Opt. Express* **15,** 16681–16689 (2007).
47. Myers, J. A.; Lewis, K. L.; Tekavec, P. F.; Ogilvie, J. P. Two-color two-dimensional Fourier transform electronic spectroscopy with a pulse-shaper. *Opt. Express* **16,** 17420–17428 (2008).
48. Eisele, D. M.; Arias, D. H.; Fu, X.; Bloemsma, E. A.; Steiner, C. P.; Jensen, R. A.; Rebentrost, P.; Eisele, H.; Tokmakoff, A.; Lloyd, S.; *et al.* Robust excitons inhabit soft supramolecular nanotubes. *Proc. Natl. Acad. Sci.* **111,** E3367–E3375 (2014).
49. Süß, J.; Wehner, J.; Dostál, J.; Brixner, T.; Engel, V. Mapping of exciton–exciton annihilation in a molecular dimer via fifth-order femtosecond two-dimensional spectroscopy. *J. Chem. Phys.* **150,** 104304 (2019).
50. Whitesides, G. M. The origins and the future of microfluidics. *Nature* **442,** 368–373 (2006).
51. Terry, S. C.; Jerman, J. H.; Angell, J. B. A gas chromatographic air analyzer fabricated on a silicon wafer. *Electron Devices, IEEE Trans.* **26,** 1880–1886 (1979).
52. Dittrich, P. S.; Manz, A. Lab-on-a-chip: microfluidics in drug discovery. *Nat. Rev. Drug Discov.* **5,** 210–218

(2006).
53. Visaveliya, N. R.; Leishman, C. W.; Ng, K.; Yehya, N.; Tobar, N.; Eisele, D. M.; Köhler, J. M. Surface Wrinkling and Porosity of Polymer Particles toward Biological and Biomedical Applications. *Adv. Mater. Interfaces* **4,** 1700929 (2017).
54. Cecchini, M. P.; Hong, J.; Lim, C.; Choo, J.; Albrecht, T.; deMello, A. J.; Edel, J. B. Ultrafast Surface Enhanced Resonance Raman Scattering Detection in Droplet-Based Microfluidic Systems. *Anal. Chem.* **83,** 3076–3081 (2011).
55. Beebe, D. J.; Mensing, G. A.; Walker, G. M. Physics and applications of microfluidics in biology. *Annu. Rev. Biomed. Eng.* **4,** 261–286 (2002).
56. DeMello, A. J. Control and detection of chemical reactions in microfluidic systems. *Nature* **442,** 394–402 (2006).
57. Song, H.; Chen, D. L.; Ismagilov, R. F. Reactions in droplets in microfluidic channels. *Angew. Chemie Int. Ed.* **45,** 7336–7356 (2006).
58. Teh, S.-Y.; Lin, R.; Hung, L.-H.; Lee, A. P. Droplet microfluidics. *Lab Chip* **8,** 198–220 (2008).
59. Sorrenti, A.; Rodriguez-Trujillo, R.; Amabilino, D. B.; Puigmartí-Luis, J. Milliseconds make the difference in the far-from-equilibrium self-assembly of supramolecular chiral nanostructures. *J. Am. Chem. Soc.* **138,** 6920–6923 (2016).
60. Arnon, Z. A.; Vitalis, A.; Levin, A.; Michaels, T. C. T.; Caflisch, A.; Knowles, T. P. J.; Adler-Abramovich, L.; Gazit, E.; Lehn, J.-M.; Brunsveld, L.; *et al.* Dynamic microfluidic control of supramolecular peptide self-assembly. *Nat. Commun.* **7,** 13190 (2016).
61. Sevim, S.; Sorrenti, A.; Franco, C.; Furukawa, S.; Pané, S.; Demello, A. J.; Puigmartí-Luis, J. Self-assembled materials and supramolecular chemistry within microfluidic environments: From common thermodynamic states to non-equilibrium structures. *Chemical Society Reviews* **47,** 3788–3803 (2018).
62. Psaltis, D.; Quake, S. R.; Yang, C. Developing optofluidic technology through the fusion of microfluidics and optics. *Nature* **442,** 381–386 (2006).
63. Chan, K. L. A.; Niu, X.; de Mello, A. J.; Kazarian, S. G. Rapid prototyping of microfluidic devices for integrating with FT-IR spectroscopic imaging. *Lab Chip* **10,** 2170–2174 (2010).
64. Chan, K. L. A.; Niu, X.; DeMello, A. J.; Kazarian, S. G. Generation of chemical movies: FT-IR spectroscopic imaging of segmented flows. *Anal. Chem.* **83,** 3606–3609 (2011).
65. Kalkman, G. A.; Zhang, Y.; Monachino, E.; Mathwig, K.; Kamminga, M. E. H. E.; Pourhossein, P.; Oomen, P. E.; Stratmann, S. A.; Zhao, Z.; van Oijen, A. M.; *et al.* Bisecting Microfluidic Channels with Metallic Nanowires Fabricated by Nanoskiving. *ACS Nano* **10,** 2852–2859 (2016).
66. Benz, C.; Retzbach, H.; Nagl, S.; Belder, D. Protein–protein interaction analysis in single microfluidic droplets using FRET and fluorescence lifetime detection. *Lab Chip* **13,** 2808 (2013).
67. Maillot, S.; Carvalho, A.; Vola, J.-P.; Boudier, C.; Mély, Y.; Haacke, S.; Léonard, J. Out-of-equilibrium biomolecular interactions monitored by picosecond fluorescence in microfluidic droplets. *Lab Chip* **14,** 1767–1774 (2014).
68. Tracy, K. M.; Barich, M. V.; Carver, C. L.; Luther, B. M.; Krummel, A. T. High-Throughput Two-Dimensional Infrared (2D IR) Spectroscopy Achieved by Interfacing Microfluidic Technology with a High Repetition Rate 2D IR Spectrometer. *J. Phys. Chem. Lett.* **7,** 4865–4870 (2016).
69. Trebbin, M.; Steinhauser, D.; Perlich, J.; Buffet, A.; Roth, S. V; Zimmermann, W.; Thiele, J.; Förster, S. Anisotropic particles align perpendicular to the flow direction in narrow microchannels. *Proc. Natl. Acad. Sci.* **110,** 6706–6711 (2013).
70. Mitchell, P. Microfluidics-downsizing large-scale biology. *Nat. Biotechnol.* **19,** 717–721 (2001).
71. Yamada, S.; Bouley Ford, N. D.; Keller, G. E.; Ford, W. C.; Gray, H. B.; Winkler, J. R. Snapshots of a protein folding intermediate. *Proc. Natl. Acad. Sci.* **110,** 1606–1610 (2013).
72. von Berlepsch, H.; Regenbrecht, M.; Daehne, S.; Kirstein, S.; Böttcher, C. Surfactant-Induced Separation of Stacked J-Aggregates. Cryo-Transmission Electron Microscopy Studies Reveal Bilayer Ribbons. *Langmuir* **18,** 2901–2907 (2002).
73. von Berlepsch, H.; Kirstein, S.; Hania, R.; Pugžlys, A.; Böttcher, C. Modification of the nanoscale structure of the J-aggregate of a sulfonate-substituted amphiphilic carbocyanine dye through incorporation of surface-active additives. *J. Phys. Chem. B* **111,** 1701–1711 (2007).
74. von Berlepsch, H.; Kirstein, S.; Böttcher, C. Effect of alcohols on J-aggregation of a carbocyanine dye. *Langmuir* **18,** 7699–7705 (2002).
75. von Berlepsch, H.; Kirstein, S.; Böttcher, C. Controlling the helicity of tubular J-aggregates by chiral alcohols. *J. Phys. Chem. B* **107,** 9646–9654 (2003).
76. Lane, N. The unseen World: Reflections on Leeuwenhoek (1677) 'Concerning little animals'. *Philosophical Transactions of the Royal Society B: Biological Sciences* **370,** 20140344 (2015).
77. The Nobel Prize in Physics 1953. Available at: https://www.nobelprize.org/prizes/physics/1953/summary/. (Accessed: 3rd December 2019)
78. Moerner, W. E.; Kador, L. Optical detection and spectroscopy of single molecules in a solid. *Phys. Rev. Lett.* **62,** 2535 (1989).
79. Orrit, M.; Bernard, J. Single pentacene molecules detected by fluorescence excitation in a p-terphenyl crystal.

Phys. Rev. Lett. **65,** 2716 (1990).
80. Brixner, T.; Hildner, R.; Köhler, J.; Lambert, C.; Würthner, F. Exciton Transport in Molecular Aggregates - From Natural Antennas to Synthetic Chromophore Systems. *Adv. Energy Mater.* **7,** 1700236 (2017).
81. Kondo, T.; Chen, W. J.; Schlau-Cohen, G. S. Single-Molecule Fluorescence Spectroscopy of Photosynthetic Systems. *Chem. Rev.* **117,** 860–898 (2017).
82. Lang, E.; Sorokin, A.; Drechsler, M.; Malyukin, Y. V.; Köhler, J. Optical Spectroscopy on Individual amphi-PIC J-Aggregates. *Nano Lett.* **5,** 2635–2640 (2005).
83. Lin, H.; Camacho, R.; Tian, Y.; Kaiser, T. E.; Würthner, F.; Scheblykin, I. G. Collective fluorescence blinking in linear J-aggregates assisted by long-distance exciton migration. *Nano Lett.* **10,** 620–626 (2010).
84. Streiter, M.; Krause, S.; von Borczyskowski, C.; Deibel, C. Dynamics of Single-Molecule Stokes Shifts: Influence of Conformation and Environment. *J. Phys. Chem. Lett.* **7,** 4281–4284 (2016).
85. Günther, L. M.; Jendrny, M.; Bloemsma, E. A.; Tank, M.; Oostergetel, G. T.; Bryant, D. A.; Knoester, J.; Köhler, J. Structure of Light-Harvesting Aggregates in Individual Chlorosomes. *J. Phys. Chem. B* **120,** 5367–5376 (2016).
86. Günther, L. M.; Löhner, A.; Reiher, C.; Kunsel, T.; Jansen, T. L. C.; Tank, M.; Bryant, D. A.; Knoester, J.; Köhler, J. Structural Variations in Chlorosomes from Wild-Type and a bchQR Mutant of Chlorobaculum tepidum Revealed by Single-Molecule Spectroscopy. *J. Phys. Chem. B* **122,** 6712–6723 (2018).
87. Löhner, A.; Kunsel, T.; Röhr, M. I. S.; Jansen, T. L. C.; Sengupta, S.; Würthner, F.; Knoester, J.; Köhler, J. Spectral and Structural Variations of Biomimetic Light-Harvesting Nanotubes. *J. Phys. Chem. Lett.* **10**, 2715–2724 (2019).
88. Schlau-Cohen, G. S.; Yang, H.-Y.; Krüger, T. P. J.; Xu, P.; Gwizdala, M.; van Grondelle, R.; Croce, R.; Moerner, W. E. Single-Molecule Identification of Quenched and Unquenched States of LHCII. *J. Phys. Chem. Lett.* **6,** 860–867 (2015).
89. Clark, K. A.; Krueger, E. L.; Vanden Bout, D. A. Direct measurement of energy migration in supramolecular carbocyanine dye nanotubes. *J. Phys. Chem. Lett.* **5,** 2274–2282 (2014).
90. Haedler, A. T.; Kreger, K.; Issac, A.; Wittmann, B.; Kivala, M.; Hammer, N.; Köhler, J.; Schmidt, H. W.; Hildner, R. Long-range energy transport in single supramolecular nanofibres at room temperature. *Nature* **523,** 196–199 (2015).
91. Jin, X.-H.; Price, M. B.; Finnegan, J. R.; Boott, C. E.; Richter, J. M.; Rao, A.; Menke, S. M.; Friend, R. H.; Whittell, G. R.; Manners, I. Long-range exciton transport in conjugated polymer nanofibers prepared by seeded growth. *Science* **360,** 897–900 (2018).
92. Kim, T.; Ham, S.; Lee, S. H.; Hong, Y.; Kim, D. Enhancement of exciton transport in porphyrin aggregate nanostructures by controlling the hierarchical self-assembly. *Nanoscale* **10,** 16438–16446 (2018).
93. Abbe, E. Beiträge zur Theorie des Mikroskops und der mikroskopischen Wahrnehmung. *Arch. für mikroskopische Anat.* **9,** 413–418 (1873).
94. Novotny, L.; Hecht, B. *Principles of Nano-Optics*. (Cambridge University Press, 2006).
95. The Nobel Prize in Physics 1986. Available at: https://www.nobelprize.org/prizes/physics/1986/summary/. (Accessed: 15th November 2019)
96. Reimer, L.; Kohl, H. *Transmission Electron Microscopy*. (Springer, 2008).
97. Bartesaghi, A.; Merk, A.; Banerjee, S.; Matthies, D.; Wu, X.; Milne, J. L. S.; Subramaniam, S. 2.2 Å resolution cryo-EM structure of β-galactosidase in complex with a cell-permeant inhibitor. *Science* **348,** 1147–1151 (2015).
98. Ganapathy, S.; Oostergetel, G. T.; Wawrzyniak, P. K.; Reus, M.; Chew, A. G. M.; Buda, F.; Boekema, E. J.; Bryant, D. A.; Holzwarth, A. R.; de Groot, H. J. M. Alternating syn-anti bacteriochlorophylls form concentric helical nanotubes in chlorosomes. *Proc. Natl. Acad. Sci.* **106,** 8525–8530 (2009).
99. von Berlepsch, H.; Böttcher, C.; Daehne, L. Structure of J-aggregates of pseudoisocyanine dye in aqueous solution. *J. Phys. Chem. B* **104,** 8792–8799 (2000).
100. Kirstein, S.; von Berlepsch, H.; Böttcher, C.; Burger, C.; Ouart, A.; Reck, G.; Daehne, S. Chiral J-Aggregates Formed by Achiral Cyanine Dyes. *ChemPhysChem* **1,** 146–150 (2000).
101. von Berlepsch, H.; Ludwig, K.; Kirstein, S.; Böttcher, C. Mixtures of achiral amphiphilic cyanine dyes form helical tubular J-aggregates. *Chem. Phys.* **385,** 27–34 (2011).
102. The Nobel Prize in Chemistry 2017. Available at: https://www.nobelprize.org/prizes/chemistry/2017/summary/. (Accessed: 15th November 2019)
103. Stenn, K.; Bahr, G. F. Specimen damage caused by the beam of the transmission electron microscope, a correlative reconsideration. *J. Ultrastruct. Res.* **31,** 526–550 (1970).
104. Glaeser, R. M.; Taylor, K. A. Radiation damage relative to transmission electron microscopy of biological specimens at low temperature: a review. *J. Microsc.* **112,** 127–138 (1978).
105. Meents, A.; Gutmann, S.; Wagner, A.; Schulze-Briese, C. Origin and temperature dependence of radiation damage in biological samples at cryogenic temperatures. *Proc. Natl. Acad. Sci.* **107,** 1094–1099 (2010).
106. Eisele, D. M.; Cone, C. W.; Bloemsma, E. A.; Vlaming, S. M.; van der Kwaak, C. G. F.; Silbey, R. J.; Bawendi, M. G.; Knoester, J.; Rabe, J. P.; Vanden Bout, D. A. Utilizing redox-chemistry to elucidate the nature of exciton transitions in supramolecular dye nanotubes. *Nat. Chem.* **4,** 655–662 (2012).
107. Kriete, B.; Bondarenko, A. S.; Jumde, V. R.; Franken, L. E.; Minnaard, A. J.; Jansen, T. L. C.; Knoester, J.; Pshenichnikov, M. S. Steering Self-Assembly of Amphiphilic Molecular Nanostructures via Halogen Exchange.

J. Phys. Chem. Lett. **8,** 2895–2901 (2017).
108. Megow, J.; Röhr, M. I. S.; Schmidt am Busch, M.; Renger, T.; Mitrić, R.; Kirstein, S.; Rabe, J. P.; May, V. Site-dependence of van der Waals interaction explains exciton spectra of double-walled tubular J-aggregates. *Phys. Chem. Chem. Phys.* **17,** 6741–6747 (2015).
109. Frederix, P. W. J. M.; Idé, J.; Altay, Y.; Schaeffer, G.; Surin, M.; Beljonne, D.; Bondarenko, A. S.; Jansen, T. L. C.; Otto, S.; Marrink, S. J. Structural and Spectroscopic Properties of Assemblies of Self-Replicating Peptide Macrocycles. *ACS Nano* **11,** 7858–7868 (2017).
110. Haverkort, F.; Stradomska, A.; de Vries, A. H.; Knoester, J. Investigating the Structure of Aggregates of an Amphiphilic Cyanine Dye with Molecular Dynamics Simulations. *J. Phys. Chem. B* **117,** 5857–5867 (2013).
111. Haverkort, F.; Stradomska, A.; Knoester, J. First-Principles Simulations of the Initial Phase of Self-Aggregation of a Cyanine Dye: Structure and Optical Spectra. *J. Phys. Chem. B* **118,** 8877–8890 (2014).
112. Frederix, P. W. J. M.; Patmanidis, I.; Marrink, S. J. Molecular simulations of self-assembling bio-inspired supramolecular systems and their connection to experiments. *Chem. Soc. Rev.* **47,** 3470–3489 (2018).

[This page was intentionally left blank]